aerospace

MDPI

Article

A Contrail Life Cycle Model with Interaction of Overlapping Contrails

Judith Rosenow [1,*] **and Mingchuan Luo** [2]

[1] Environmental Impact and Sensor Technology Department, DLR German Aerospace Center, 03046 Cottbus, Germany
[2] Institute of Logistics and Aviation, Technische Universität Dresden, 01069 Dresden, Germany; mingchuan.luo@tu-dresden.de
* Correspondence: judith.rosenow@dlr.de; Tel.: +49-355-28888-191

Abstract

Air transport, acknowledged as the safest and most efficient mode for long-haul travel, is confronted with diverse challenges aimed at improving its environmental performance. A notable aspect of this effort involves the formation of contrails, arising from the emission of water vapor and condensation nuclei in a cold, ice-supersaturated atmosphere, which represents one of the most difficult-to-predict yet physically quantifiable environmental impacts of air traffic. Adopting the bottom-up principle to evaluate individual contrails for trajectory optimization introduces uncertainties in calculating the radiative forcing of contrails and modeling their life cycle. Former studies for modeling the microphysical life cycle of individual contrails based on a 2D Gaussian plume model could be validated with a photographic contrail tracking method in the mid-latitudes. However, contrails rarely form individually over Central Europe; rather, they form as an accumulation behind many aircraft flying through an ice-supersaturated region. For this reason, the 3D Gaussian plume model has been extended for the co-existence of several contrails. The greater the overlap of the contrails, the greater the competition in ice supersaturation between the contrails and therefore the greater the reduction in lifetime compared to single contrails. Furthermore, with increasing overlap, the number density of ice crystals increases, resulting in smaller ice crystals with shorter lifetimes. The overlap effect is also reflected in the angle between non-parallel contrails. The results can be used for further studies on the optical properties of real co-existing contrails.

Keywords: contrails; microphysics; life cycle; aviation non-CO_2 effects

Academic Editor: Miroslav Kelemen

Received: 22 December 2025
Revised: 5 February 2026
Accepted: 6 February 2026
Published: 10 February 2026

1. Introduction

Operational developments in aviation sometimes suffer from the strict, multi-criteria objectives of international organizations such as the Single European Sky (SES) initiative launched in 1999 and associated research institutions such as the SES Air Traffic Management Research (SESAR) group. As laid down in Article 100(2) of the Treaty on the Functioning of the European Union, new developments in the aviation sector must not only increase safety and cost efficiency but also reduce the environmental impact by at least 10%. To achieve this, the environmental impact of both individual flights and the entire air transport system must first be quantified and monitored. Contrails, caused by the emission of water vapor and condensation nuclei in an ice-supersaturated and cold atmosphere [1,2] play a particularly volatile role in these endeavors. Their formation, lifetime, and effects on

the Earth's energy budget depend on numerous factors [1,2]. Predicting, monitoring, and post-analyzing them has posed particular challenges for scientists for decades [3].

Scaling represents a major challenge. From a global perspective, contrails are often regarded as infinitely extended cloud cover, and their radiative impact is assessed globally accordingly [4] or in the spatial and temporal resolution of geostationary satellites [5]. Both do not allow detailed operational findings for the optimization of individual flights. On the other hand, when the lifetime and optical characteristics of contrails are evaluated on a single-flight basis, the effects of co-existing contrails on their lifetime and radiative properties are not taken into account [6]. However, when we observe the sky, we often see numerous overlapping contrails without them forming a homogeneous cloud cover.

In this paper, a physical model for calculating the microphysical properties of individual contrails along the life cycle [7] is extended to calculate the impact of co-existing contrails on their lifetimes. Therefore, the most important input variables for the optical properties of co-existing contrails can be provided.

2. State of the Art

Numerous studies focusing on measuring or tracking contrails from the ground or space give valuable insides in contrail microphysics and lifetime but do not distinguish between single or multiple co-existing contrails [8–13]. Thereby, various methods are employed to analyze the contrail life cycle utilizing satellite observations, a method becoming applicable only once the contrail reaches full development, entering the dissipation regime [8,9,12,14], because satellite observation validity is contingent on the contrail manifesting as a line-shaped artificial cirrus cloud in the atmosphere, particularly when detected automatically [10–12]. Wang et al. [15] delved further into the microphysical properties of satellite-observed contrails. Their examination of an effective radius, particle number density, and optical thickness between contrails, contrail cirrus, and natural cirrus, based on in situ measurements, revealed smaller particle radii in contrails than in natural cirrus. However, a distinction between the properties of single and grouped contrails has not been made. Geraedts et al. [16] developed an automated detection and matching system that uses satellite data to determine whether individual flights have produced persistent contrails, aiming to improve contrail prediction methods, while Wang [17] focuses on aircraft contrail detection in global satellite images using semantic segmentation based on the Unified Perceptual Parsing for Scene Understanding (UPerNet) architecture. The approach utilizes two ConvNeXt (a Convolutional Network) configurations to improve performance and a cross-entropy loss with positive-class weights to enhance contrail recognition.

Another assessment technique involves microphysical models, e.g., Contrail Cirrus Prediction Tool (COCiP) describing the individual contrail life cycle as a Lagrangian Gaussian plume [18]. This model characterizes averaged particle properties of individual contrails, neglecting interaction with the atmosphere [18], despite detailed observations on contrail lifetime and optical properties published by Schumann and Heymsfield in 2007 [19]. The contrail lifetime is therefore strongly parameterized in COCiP. Cantin et al. [20] demonstrate the feasibility of coupling Eulerian–Lagrangian Comuptational Fluid Daynamics (CFD) with ice microphysics to predict near-field contrail formation. The study focuses on the initial stages of single contrail development, emphasizing the dynamics of trailing wake vortices and their influence on microphysical processes. Pauen et al. [21] investigate the initial stage of the contrail life cycle. The research employs high-fidelity CFD simulations to analyze the impact of various parameters, such as relative humidity and thermal stratification, on contrail evolution. Unfortunately, the method is not described comprehensively. Finally, Ramsay et al. [22] integrates a contrail microphysics model within Reynolds-Averaged Navier–Stokes (RANS) simulations to assess the environmental impact of aircraft

design on contrail formation. The study examines how different aircraft configurations influence ice crystal formation, growth, and dynamics within contrails. Unfortunately, all these studies focus on the early evolution of single very young contrails and do not consider the entire contrail's lifetime or contrails, which may be embedded in artificial or natural cloud cover. While not primarily intended for modeling individual contrail life cycles, a few in situ [23] and remote sensing measurements [24] of contrails are valuable for approximating typical lifetimes and can aid in model validation. A research aircraft equipped with cloud microphysics probes and remote sensing instruments was flown in an ice-supersaturated region to gather such data. Sampling contrails aged between 7 and 30 min, this approach considered the critical timeframe for optimal ice particle observation, extending to the point where typical mid-latitude contrails are no longer present. The contrail life cycle, identified through in-flight Lidar measurements, was later modeled and compared with the UK Met Office NAME III climate model [25]. While these measurements offer valuable insights and could be applied to single and multiple co-existing contrails, the logistical challenges restrict their ability to comprehensively cover all atmospheric conditions influencing contrail lifetime over the long term.

Another promising method of investigating contrail life cycles is measurements of artificially generated contrails in cloud chambers, such as the Aerosol Interaction and Dynamics in the Atmosphere (AIDA) chamber, which simulates atmospheric processes by modifying aerosols physically and chemically. The accuracy of ice-nucleation control in AIDA is already validated through measurements of homogeneous freezing at approximately −34 °C [26]. Extending the measurement environment to temperatures around −56 °C would provide ideal conditions for contrails and deliver promising results.

Predicting the occurrence and persistence of contrails remains a challenge due to the strong sensitivity to small-scale atmospheric conditions. While empirical and physics-based models can capture formation probability reasonably well under idealized conditions, their skill in forecasting long-lived contrails in operational settings is limited by uncertainties in humidity and temperature fields [18,27]. Beyond simple contrail avoidance, modest adjustments in flight altitude have been shown to significantly reduce contrail climate forcing when suitable ice-supersaturated regions are avoided, although this may conflict with fuel optimality [28]. Persistent contrails are strongly dependent on meteorological situations characterized by low temperatures and high ice supersaturation, often associated with upper-tropospheric fronts and cirrus regimes [29]. Conditions such as increased relative humidity with respect to ice and weak vertical wind shear are particularly conducive to contrail persistence [30]. Preliminary conceptual studies on hydrogen aircraft design suggest that zero persistent contrails may be achievable through reduced water vapor emissions and optimized plume dynamics, although this remains sensitive to cruise altitude and ambient humidity [31]. The use of sustainable aviation fuels has been shown to alter soot emissions, thereby affecting contrail formation thresholds and microphysical properties, potentially reducing contrail occurrence and radiative forcing [32]. Innovative aircraft configurations, such as box-wing designs, may alter wake structure and emissions distribution, with implications for contrail coverage and climate impact that are still under investigation [33]. Hybrid-electric propulsion concepts are also expected to influence contrail coverage through changes in emission indices and flight patterns, though quantitative assessments remain scarce [34]. Recent advances in linear temperature response modeling provide a framework for characterizing the full climate impact of individual flights, integrating CO_2 and non-CO_2 effects in a consistent manner [35]. Finally, progress in contrail observation and tracking using geostationary satellite data combined with air traffic trajectories has enabled the improved validation of contrail predictions and a better understanding of contrail evolution in real airspace [36].

This literature review highlights the challenges associated with determining contrail lifetime and its microphysical properties, which depend on numerous highly variable and non-continuous atmospheric factors. Consequently, many studies are constrained to establishing averaged or typical lifetimes for either individual contrails or infinitely extended contrail cover. Conversely, global observations offer the advantage of tracking the entire evolution of contrails and the non-linear shape of aviation-induced cloudiness. In response to this challenge, our approach focuses on achieving the most precise determination of the atmospheric state and subsequently calculating the lifetime of co-existing contrails based solely on physical laws.

3. Microphysical Lifetime Modeling for Single Contrails

3.1. Initial Contrail Dimensions and Decay

Our approach is based on an extension of the already validated Gaussian plume model [36,37] to calculate individual condensation trails in a cloudless atmosphere [7]. On average, a contrail lifetime accuracy of 90% was achieved, although this accuracy may have been limited by radiosonde measurement uncertainties and lateral wind drift. To do this, the life cycle is divided into the following four phases [38]: In the jet regime, the engine emissions are captured between two counter-rotating vortices (developed at the rear of the wings, resulting in swirling air masses trailing downstream of the wing tips) forming the primary wake. In the subsequent vortex regime, the primary wake descends due to a substantial gradient in ambient density, forming a secondary wake. The aircraft engine emissions become captured between the continuously generated primary wake at flight altitude and the secondary wake below flight altitude. Approximately 100 s after emission (denoted as t_{diss} [s], as estimated by Holzäpfel et al. [39]), the turbulence in both wakes decays, allowing exhaust gases to escape the curtain between the primary and secondary wakes. In this newly initiated dissipation regime, both wakes continue to decay. Ice particles can grow to a sufficient size to persist through this regime only in an ice-supersaturated atmosphere. Over the subsequent hours, the exhaust undergoes diffusion in the diffusion regime, facilitating the mixing of emissions with the surrounding ambient atmosphere.

From this, it follows that the initial dimensions of the contrail in the diffusion regime depend on the descending time t_{diss} of the primary wake, as well as the horizontal dimensions of the wake vortices at the end of the dissipation regime. While the initial height of the contrail c_v [m] is calculated using the probabilistic wake vortex model [39], the initial width of the contrail c_h [m] is determined by the aircraft geometry (e.g., wingspan) [7].

Subsequently, the contrail lifetime in the diffusion regime is modeled using the Gaussian plume model, where the contrail gradually diffuses into the ambient atmosphere. To represent this process, a Gaussian distribution is applied along both the vertical and horizontal axes. The standard deviation is defined as the point where the tangential velocity of the vortices decreases to $(\sqrt{e})^{-1}$ of its maximum value at the vortex center [40].

Figure 1 illustrates two 2D Gaussian distribution functions and defines the axes used in this model.

Due to the 2D Gaussian distribution function, the ice mass concentration decreases with distance from the center, as expected in real fluids mixing with another fluid. Based on this assumption, vortex-centric ellipses are generated, each with a constant ice mass. The Ice Water Content (IWC), expressed in kg m^{-3}, is used to represent the total ice mass per unit volume of the contrail.

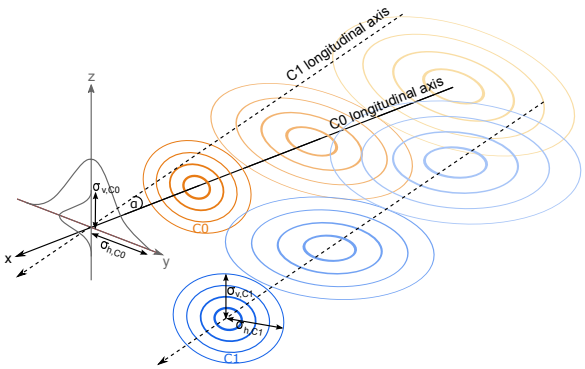

Figure 1. Overlapping two 2D Gaussian plume models representing two contrails. The flight paths are shown along the x-axis, with time increasing in the downstream direction. Orange and blue colors indicate two different contrails, whose spatial overlap is highlighted. Older stages of the contrails are represented by progressively paler ellipses.

The two-dimensional probability density function provides the number of ice particles in the contrail at any given time t [s] and place:

$$f(\vec{x}, t) = \frac{1}{2\,\pi\sqrt{\det\hat{\sigma}(t)}}\exp\left[-\frac{1}{2}\,\vec{x}^{T}\,\hat{\sigma}(t)^{-1}\,\vec{x}\right], \tag{1}$$

where $\vec{x}$ describes the position vector

$$\vec{x} = \begin{pmatrix} y \\ z \end{pmatrix} \tag{2}$$

In Equation (1), the variance in the standard deviation $\hat{\sigma}(t)$ [m^2] is characterized by a matrix encompassing horizontal $\hat{\sigma}_h(t)$ [m], vertical $\hat{\sigma}_v(t)$ [m], and sheared $\hat{\sigma}_s(t)$ [m] components, representing the diffusion of the contrail.

$$\hat{\sigma}(t) = \begin{pmatrix} \hat{\sigma}_h(t) & \hat{\sigma}_s(t) \\ \hat{\sigma}_s(t) & \hat{\sigma}_v(t) \end{pmatrix} \tag{3}$$

The evolution of the variances $\hat{\sigma}_h(t)$, $\hat{\sigma}_v(t)$, and $\hat{\sigma}_s(t)$ is described by the following relationship [37]:

$$\hat{\sigma}_h(t) = \frac{2}{3}sh^2\,D_v\,t^3 + (2\,D_s + sh\,\sigma_{0v}^2)sh\,t^2 + 2\,D_h\,t + \sigma_{0h}^2 \tag{4}$$

$$\hat{\sigma}_s(t) = sh\,D_v\,t^2 + (2\,D_s + sh\,\sigma_{ov}^2)\,t \tag{5}$$

$$\hat{\sigma}_v(t) = sh\,D_v\,t + \sigma_{ov}^2, \tag{6}$$

where sh [s^{-1}]

$$sh = \frac{\Delta v}{\Delta z} \tag{7}$$

denotes wind shear as the difference in wind speed Δv [m s^{-1}] between two altitudes Δz [m].

In Equations (4)–(6), D_v, D_h, and D_s are the components of an asymmetric and anisotropic diffusivity tensor:

$$\hat{D} = \begin{pmatrix} D_h & D_s \\ D_s & D_v \end{pmatrix}. \tag{8}$$

D_v, D_h, and D_s depend on atmospheric stratification, turbulence, and wind shear [7].

Due to diffusion, the contrail cross-section will gradually increase and the distribution of the IWC_s in the contrail cross-section follows the two-dimensional Gaussian distribution, as derived from Equation (1).

Considering the area of an ellipse [41], the contrail cross-section CCS [m^2] is defined as

$$A = 2\,\pi\sqrt{\det\sigma} \tag{9}$$

and the initial standard deviations $\sigma_{0h} = c_h/2.2$ and $\sigma_{0v} = c_v/2.2$ are defined as starting values for the diffusion regime [37], where c_h [m] and c_v [m] are the width and height of the contrail, respectively. This means that the standard deviations are multiplied by 2.2 in order to estimate the total contrail extent.

Based on these elaborations, Equation (1) is solved as follows:

$$f(y,z,t,D_v,D_h,D_s) = \frac{1}{2\pi\sqrt{\det\hat{\sigma}(t)}}\exp\left[-\frac{1}{2\det\hat{\sigma}(t)}(\hat{\sigma}_v(t)\,y^2 + \hat{\sigma}_h(t)z^2)\right] \tag{10}$$

3.2. Single Contrail Microphysics

The lifetime of the contrail is defined by two limiting parameters, namely $IWC < 10^{-8}$ kg m^{-3} or $rH_{\text{ice}} < 100\%$ [18]. In the case of $IWC < 10^{-8}$ kg m^{-3}, the contrail reaches a hypothetical state where it becomes too optically thin to be visibly identified. Therefore, the IWC is calculated at each time step according to Equation (14). In the case of $rH_{\text{ice}} < 100\%$, the contrail experiences sublimation as it moves away from the ice-supersaturated region. For this criterion, the rH_{ice} (Equation (11)) is calculated at each time step. Since the small ice crystals occupy only a small fraction of the large contrail volume, it can be assumed that they sublimate very rapidly once the contrail volume is no longer ice-supersaturated.

Assuming a constant vapor pressure above ice e_{ice} and water e_{water}, the relative humidity above ice is

$$rH_{\text{ice}} = \frac{e_{\text{ice}}}{e^*_{\text{ice}}} = rH_{\text{water}}\frac{e^*_{\text{water}}}{e^*_{\text{ice}}}, \tag{11}$$

where rH_{water} is provided by weather data and e^*_{water} and e^*_{ice} are functions of atmospheric temperature [42]. The amount of vapor pressure above saturation Δe is assumed to be captured by the ice particles

$$\Delta e = e^*_{\text{ice}}\left(\frac{rH_{\text{ice}}}{100} - 1\right). \tag{12}$$

The amount of IWC above saturation IWC_s contributing to the ice particle size is

$$IWC_s = \frac{\Delta e}{R_v\,T}, \tag{13}$$

where $R_v = 461.5$ J(kg K)$^{-1}$ represents the specific gas constant for water vapor. The distinction of IWC_s from the total IWC lies in the fact that IWC_s pertains to humidity, which is not essential for saturating the air within the contrail and can thus contribute to the growth of ice particles.

The total IWC of the ice particles within a segment of the contrail is determined by the distance s flown by the aircraft in one second (i.e., true airspeed v_{TAS} [m s^{-1}]), the emission index of water vapor by the engine $EI_{\text{water}} = 1.24$ kg kg^{-1} [43] and the contrail cross-section CCS

$$IWC = IWC_s + EI_{\text{water}}\frac{m_f}{v_{\text{TAS}}\,CCS}. \tag{14}$$

The amount of available ice mass m_{ice} [kg]

$$m_{\text{ice}} = IWC \cdot CCS \cdot s \tag{15}$$

enables the calculation of the volume V_p [m^3] of a spherical ice particle

$$V_p = \frac{\pi}{6} d_p^3 = \frac{IWC}{N_{\text{ice}}\,\rho_{\text{ice}}}, \tag{16}$$

where $\rho_{\text{ice}} = 917\ \text{kg}\,\text{m}^{-3}$ denotes the density of ice [44] and d_p [m] denotes the ice particle diameter.

The fuel flow $\dot{m}_f$ [kg s^{-1}] determines the initial number of ice crystals (corresponding to the number of emitted hydrophilic soot particles, which is $N_{\text{ice}} = 10^{15}$ per kg of combusted kerosene [45]). A constant average number of ice particles is assumed, as the probabilities of aggregation and shattering remain low and comparable at low temperatures [46]. Consequently, the initial mean crystal diameter is

$$d_p = \sqrt[3]{\frac{6\,m_{\text{ice}}}{\pi\,N_{\text{ice}}\,\rho_{\text{ice}}}}. \tag{17}$$

3.3. Vertical Dynamics of Single Contrails

Each ice particle experiences a drag force as a result of viscous friction [47]. From this follows a contrail sedimentation speed [m s^{-1}]

$$v_{\text{s,p}} = \frac{2\,r_p^2\,\rho_p\,g}{9\,\eta_{\text{dyn}}} \tag{18}$$

depending on ice particle radius r_p [m], ice particle density ρ_p [kg m^{-3}], and dynamical viscosity η_{dyn} [kg m^{-1}s^{-1}] [48]. The sedimentation speed $v_{\text{s,p}}$ may be influenced by a vertical movement induced by the (vertical) wind drift. If a vertical upward wind speed surpasses the sedimentation speed, the ice particles will rise. On the other hand, assuming an upward vertical wind speed of $v_z = 0.005$ m/s, Equation (18) implies that the contrail will sediment to lower, warmer, and drier altitudes once the mean radius of the ice particles exceeds $r_p \approx 6$ µm. During sedimentation, the contrail experiences adiabatic heating [40] with an impact on contrail temperature $T(t_i)$ and IWC, causing the sublimation of ice particles. As a result, the relative humidity within the contrail decreases, leading to a reduced contrail lifetime.

The change in $IWC_{\text{adiab}}(t_i)$ can be calculated as

$$IWC_{\text{adiab}}(t_i) = IWC(t_{i-1}) - \frac{e^*_{\text{ice}}(t_i) - e^*_{\text{ice}}(t_{i-1})}{R_v\,T(t_i)}. \tag{19}$$

For each time step t_i, $IWC(t_i)$ becomes

$$IWC(t_i) = \frac{IWCs(t_i) \cdot (CCS(t_i) - CCS(t_{i-1})) + IWC_{\text{adiab}}(t_i) \cdot CCS(t_{i-1})}{CCS(t_{i-1})}. \tag{20}$$

3.4. Horizontal Dynamics of Single Contrails

In addition to vertical movement, the contrail experiences horizontal drift and can potentially exit the ice-supersaturated layer. The presence of strong winds contributes to the distortion of the contrail cross-section, which is accounted for in turbulence-dependent diffusion $\hat{\sigma}_s(t)$ (see Equation (5)). In this context, the horizontal displacement aligns with the horizontal wind speed provided by the weather data.

3.5. Findings on Single Contrail Lifetime

From the model described above, the following conclusions can be drawn:

- At the very least, the contrail lives as long it stays in an ice-supersaturated region.
- The IWC, defined as ice mass per volume, depends on the growth rate of the contrail (i.e., the diffusion rate) and the degree of ice supersaturation. The IWC can decrease with rapid growth in a slightly supersaturated environment.
- As long as the contrail mixes with ice-supersaturated air by diffusion, the mean particle diameter d_p increases because the average number of ice particles remains constant. The larger the ice particles, the higher the sedimentation rate.
- Due to larger horizontal diffusivities ($D_h > D_v$), $\sigma_h > \sigma_v$ is assumed for the main part of the contrail's lifetime [40].

All assumptions made in this parametric study influence the resulting contrail lifetime. The sensitivity to the assumed shear-induced diffusivity has been investigated in [40], showing that increasing shear diffusivity leads to a reduced contrail lifetime due to enhanced turbulent mixing. Furthermore, the impact of the ice crystal number concentration on the contrail lifetime is discussed in [49]. A lower number of ice crystals results in larger mean crystal sizes, which enhances sedimentation and consequently shortens the contrail lifetime.

4. Microphysical Modeling of Overlapping Contrails

4.1. Assumptions and Case-by-Case Analysis of Embedded Contrails

The approach described in Section 3 is extended to analyze two contrails that intersect during their lifetime. To account for this interaction, the model is parallelized. The source code developed for this study is openly available at https://github.com/jro-github/intersected_contrails/tree/main (accessed on 1 November 2025), licensed under Apache-2.0. At each time step, overlapping volumes, defined as the intersection of the regions bounded by the contrail centerline and their respective horizontal and vertical standard deviations, $\hat{\sigma}_h(t)$ and $\hat{\sigma}_v(t)$ are identified. If an intersection occurs, the angle α between contrail segments C_0 and C_1 is determined. Since the modeling framework is independent of contrail orientation, α is constrained to a range of 0 to 90 degrees. The non-overlapping sections of both contrails remain distinct, while the overlapping zone is treated as a separate contrail segment without any outer surface, denoted as C_I, with its own microphysical properties and lifetime (see Figure 2).

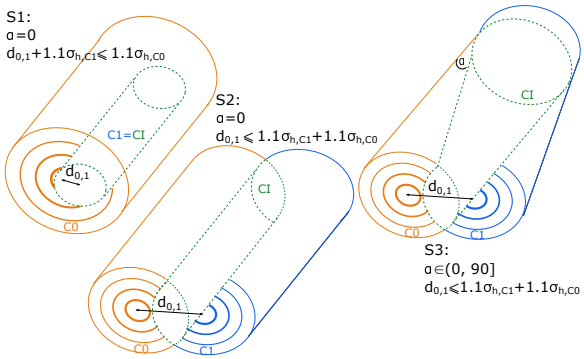

Figure 2. Three cases of contrail intersections considered in this study.

Three scenarios based on the initial angle α and the initial distance between the centers of the two contrails $d_{0,1}$ are differentiated (see Figure 2). Note that contrails will switch between scenarios during their lifetime, for example, when they separate or converge. The model distinguishes between scenarios because contrail formation and evolution are

highly non-linear: small differences in initial conditions can lead to substantially different lifetimes and optical properties. By grouping initial conditions into a few representative scenarios, the complexity of the simulation is reduced and the focus lays on the most relevant dynamics. This approach also improves the interpretability, allowing a clear comparison of the contrail behavior across different cases.

- S1: The components C_0 and C_1 are positioned in a parallel configuration, where C_1 is entirely embedded in C_0. Initially, the model calculated the lifetime of C_0 and C_1, resulting in $\alpha = 0$ and satisfying the condition $d_{0,1} + 1.1\,\sigma_{h1} \leqslant 1.1\,\sigma_{h0}$. Since only the vertical or horizontal extent in one direction from the center point is relevant here, the standard deviation is therefore multiplied by the factor 1.1.
- S2: The components C_0 and C_1 are overlapped in a parallel configuration, where C_1 is partially enclosed by C_0. The interaction zone C_I is treated as a separate contrail segment from the beginning on. $\alpha = 0$ and $1.1\,\sigma_{h1} - 1.1\,\sigma_{h0} \leqslant d_{0,1} \leqslant 1.1\,\sigma_{h1} + 1.1\,\sigma_{h0}$.
- S3: The components C_0 and C_1 are overlapped in a non-parallel configuration. Consequently, the model must account for all three components, C_I, C_0, and C_1. The defining conditions in this case are $\alpha \in (0, 90]$ and $d_{0,1} \leqslant 1.1\,\sigma_{h1} + 1.1\,\sigma_{h0}$.

Case S1 represents a scenario of two consecutively flying aircraft. Due to their local offset, contrails of different sizes but with very similar positions and longitudinal-axis orientations converge within the ice-supersaturated region.

Although case S2 ($\alpha = 0$) is formally a special case of S3 ($\alpha \in (0, 90]$), it is treated as a distinct scenario. This distinction is justified by its frequent occurrence in operational environments, which is primarily attributed to the structured airway system and commonly applied lateral offsets.

Case S3 represents the most general case, offering a flexible framework that can be adapted to accommodate any possible configuration of contrails.

4.2. Geometry of Overlapping Contrails

The distance $d_{0,1}$ between two contrail cores is determined using the Haversine formula [50].

$$d_{0,1} = 2 \cdot R \cdot \arcsin(\sqrt{a_{\text{distance}}}), \tag{21}$$

where R = 6,371,000 m is the Earth radius and a_{distance} denotes the angular distance

$$a_{\text{distance}} = \sin^2\left(\frac{\Delta\varphi}{2}\right) + \cos(\varphi_0)\cos(\varphi_1)\sin^2\left(\frac{\Delta\lambda}{2}\right). \tag{22}$$

where φ, $\Delta\varphi$, λ, and $\Delta\lambda$ [rad] denote latitude, difference in latitude, longitude, and difference in longitude of the contrail cores C_0 and C_1.

$$\Delta\varphi = \varphi_1 - \varphi_0 \tag{23}$$

$$\Delta\lambda = \lambda_1 - \lambda_0 \tag{24}$$

In the case of an interaction of contrails, the following findings are made:

- Once the contrails overlap, they may separate again. Despite being subject to the same wind conditions, variations in particle sedimentation speed can occur due to differences in ice particle diameters.
- Initially, the ice water content (IWC_{C_I}) within the interaction zone is relatively high, as it corresponds to the combined ice water content of the individual contrails IWC_{C_0} and IWC_{C_1}, weighted by their overlap volume V_{C_I}.

- The overlap volume V_{C_I} increases with time due to the symmetric growth around the center of both contrails.
- Given the initially high IWC_{C_I}, a further strong increase in IWC_{C_I} is unlikely due to the growth of C_I embedded within C_0 and C_1. C_I can only draw IWC from C_0 and C_1 and lacks contact with the surrounding ice-supersaturated atmosphere. Instead, it is more likely that IWC_{C_I} decreases over time.

The analysis of overlapping contrails is based on a continuum and statistical representation of contrails, in which ice particles are not treated individually but as a spatially distributed number density field [51]. Each contrail is assumed to exhibit a Gaussian particle distribution, reflecting the combined effects of turbulent diffusion and large-scale mixing without resolving microphysical processes. Under this assumption, the total number of particles contained in any subvolume of the contrail scales proportionally with the volume fraction of that region relative to the entire contrail [19]. The overlap between two contrails is therefore described purely geometrically: the number of ice particles within the intersection volume is assumed to be proportional to the ratio of the intersection volume to the respective contrail volumes [52]. Molecular diffusion, Brownian motion, particle–particle interactions, and sedimentation are neglected, as these processes act on much smaller spatial and temporal scales than those relevant for the considered contrail overlap and are implicitly represented by the Gaussian spread [53]. Ice particle concentrations are treated analogously to a passive scalar, assuming that the particles do not significantly influence the flow or the mixing process. Furthermore, the analysis focuses on a quasi-static snapshot of the contrail interaction, such that the temporal evolution of the overlap region is of secondary importance. Finally, ice particles in both contrails are assumed to have comparable properties, allowing the overlap to be quantified in terms of particle number without introducing additional microphysical complexities [54].

The overlap volume V_{C_I} depends on α and $d_{0,1}$. In S1,

$$V_{C_I,\,S1} = CCS_{C_I,\,S1} \cdot s, \tag{25}$$

where s [m] represents the length of the contrail section, determined by the aircraft speed and a fixed time discretization of one second, and $CCS_{C_I,\,S1}$ is the area of intersection (Equation (9)) of C_1 covered by C_0.

In S2, $CCS_{C_I,\,S2}$ is assumed as an ellipse with the semi-major axis

$$a_{C_I,\,S2} = (1.1\,\sigma_{h0} + 1.1\,\sigma_{h1} - d_{0,1})/2, \tag{26}$$

and the semi-minor axis

$$b_{C_I,\,S2} = 1.1\,\sigma_{v0} \cdot \sqrt{1 - \left[\frac{(1.1\,\sigma_{h0} - a_{C_I,\,S2})}{1.1\,\sigma_{h0}}\right]^2}. \tag{27}$$

Therefore, $CCS_{C_I,\,S2}$ can be calculated by

$$CCS_{C_I,\,S2} = \pi \cdot a_{C_I,\,S2} \cdot b_{C_I,\,S2} \tag{28}$$

and the volume overlap $V_{C_I,\,S2}$ arises from

$$V_{C_I,\,S2} = CCS_{C_I,\,S2} \cdot s. \tag{29}$$

In S3 (contrails overlap with $\alpha > 0$), the volume overlap $V_{C_I,\,S3}$ is made up of three parts, two of which are identical: two edge parts $V_{\text{top cube},\,S3}$ and one central part $V_{\text{mid cyl},\,S3}$ (see Figure 3). $V_{\text{top cube},\,S3}$ is approximated as a cone with the height:

$$h_{\text{top cube, S3}} = \begin{cases} 2.2\,\sigma_{h1} \cdot \cot\alpha & \alpha \in (0°, 90°) \\ 1.1\,\sigma_{h0} - \sqrt{(1.1\,\sigma_{h0})^2 - (1.1\,\sigma_{h1})^2} & \alpha = 90°. \end{cases} \tag{30}$$

The cone volume $V_{\text{top cube, S3}}$ is considered as

$$V_{\text{top cube, S3}} = \frac{1}{3} \cdot CCS_{C_1} \cdot h_{\text{top cube, S3}}. \tag{31}$$

The length of the middle cylinder

$$l_{\text{mid cyl, S3}} = \begin{cases} 2.2\,\sigma_{h0} \,/\, \sin\alpha - h_{\text{top cube, S3}} & \alpha \in (0°, 90°) \\ 2.2\,\sigma_{h0} - 2 \cdot h_{\text{top cube, S3}} & \alpha = 90° \end{cases} \tag{32}$$

multiplied with the contrail cross-section CCS_{C_1} is the volume of the middle cylinder:

$$V_{\text{mid cyl, S3}} = CCS_{C_1} \cdot l_{\text{mid cyl, S3}}. \tag{33}$$

The total volume of the two contrails' intersection is

$$V_{C_I, S3} = 2 \cdot V_{\text{top cube, S3}} + V_{\text{mid cyl, S3}}. \tag{34}$$

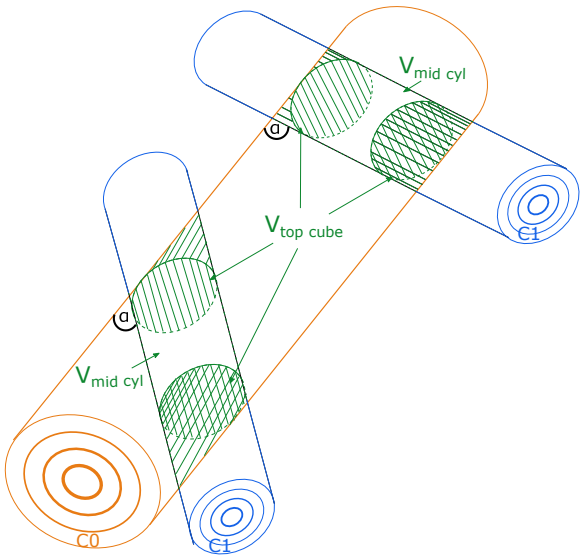

Figure 3. Components $V_{\text{top cube, S3}}$ and $V_{\text{mid cyl, S3}}$ of the volume overlap of two cylinders in S3.

The calculation of the overlapped cross-section CCS_{C_I} depends on the scenario. In S1, CCS_{C_I} equals $CCS_{C_1, S1}$ (Equation (9)). In S2, $CCS_{C_I, S2}$ is calculated by Equation (28). In S3 ($\alpha \neq 0$), CCS_{C_I} depends on intersection volume $V_{C_I, S3}$ and on intersection length $l_{C_I, S3}$:

$$l_{C_I, S3} = 2.2\,\sigma_{h0} \,/\, \sin\alpha, \qquad if\ \alpha \in (0°, 90°], \tag{35}$$

$$CCS_{C_I, S3} = \frac{V_{C_I, S3}}{l_{C_I, S3}}. \tag{36}$$

4.3. Microphysics of Embedded Contrails

For each time step, IWC is calculated as a function of Δ_e, CCS, and the amount of emitted water vapor (see Equation (14)). For the initial time step of intersection, IWC_{C_I}

is estimated as the sum of IWC_{C_0} and IWC_{C_1} which lies proportionally in the overlap in terms of volume.

$$IWC_{C_I}(t_0) = \frac{V_{C_I}}{V_{C_0}} IWC_{C_0}(t_0) + \frac{V_{C_I}}{V_{C_1}} IWC_{C_1}(t_0). \tag{37}$$

In the case of S1 (C_0 and C_1 are in parallel and C_1 is completely covered by C_0), $IWC_{C_I}(t_0)$ is determined by the sum of IWC_{C_1}, weighted by V_{C_1} compared to V_{C_0} and the water vapor emission of C_1:

$$IWC_{C_I,S1}(t_0) = \frac{V_{C_I}}{V_{C_0}} IWC_{C_0}(t_0) + EI_{\text{water}} \frac{m_f}{v_{\text{TAS}}\, CCS_{C_1}}. \tag{38}$$

For each additional time step, IWC_{C_I} depends on the type of intersection case.

For scenario S1, a transfer of a fraction of the ice mass and ice particles from C_0 to C_I, depending on the growth rate of C_I within C_0 and the volume ratio between V_{C_0} and V_{C_I}, is assumed.

$$IWC_{C_I,S1}(t_i) = IWC_{C_I,S1}(t_{i-1}) + \frac{V_{C_I}}{V_{C_0}} IWC_{C_0}(t_i). \tag{39}$$

In the cases of S2 and S3 (C_0 and C_1 have different outside surfaces, and C_I does not have an outside surface), IWC_{C_I} is initially determined by the sum of IWC_{C_0} and IWC_{C_1}, weighted according to the respective contributions of each component within the volume of the intersection (Equation (37)). Depending on the growth rate of C_0, C_1, and C_I (and the volume ratios between V_{C_0}, V_{C_1}, and V_{C_I}) part of the ice mass (and ice particles) of C_1 and C_0 is transferred to C_I:

$$IWC_{C_I,S2,S3}(t_i) = \frac{V_{C_I}}{V_{C_0}} IWC_{C_0}(t_i) + \frac{V_{C_I}}{V_{C_1}} IWC_{C_1}(t_i). \tag{40}$$

As V_{C_I} also increases here at the same time and the increase in $IWC_{C_I}(t_i)$ is expected to be lower than in $IWC_{C_0}(t_i)$ and $IWC_{C_1}(t_i)$, a decrease in IWC_{C_I} over time is expected.

Simultaneously, the ice particle diameter in C_I (d_{p,C_I}) (Equation (17)) is estimated as a function of the total ice mass in C_I (m_{ice,C_I}) and of the proportionate number of ice particles N_{ice,C_I} corresponding to V_{C_I}, compared to V_{C_0} and V_{C_1}. Note that d_p is crucial for the contrail lifetime since it determines the sedimentation speed $v_{s,p}$.

During their lifetime, the contrails undergo a transition between different geometric configurations (i.e., overlapping, partially overlapping, separated, changes in angle α) as they evolve over time. From this, it follows that the calculation basis can change between scenarios during the service life. Finally, for each time step, the geometric configuration (i.e., *S*1, *S*2, or *S*3) is determined and the sedimentation speed for C_0, C_1, and C_I (Equation (18) as a function of particle size d_p and vertical wind v_z) is calculated. Subsequently, the lifetime conditions $IWC < 10^{-8}\,\text{kg}\,\text{m}^{-3}$ or $rH_{\text{ice}} < 100\%$ are confirmed. Due to the expected slower growth rate of IWC_{C_I}, compared to IWC_{C_0} and IWC_{C_1}, a slightly lower sedimentation speed of C_I compared to C_0 and C_1 is expected.

If either C_0 or C_1 sublimates due to $rH_{\text{ice}} < 100\%$, C_I will also sublimate. In this case, the impact of the intersection on the lifetime is likely small. Conversely, if C_0 or C_1 sublimates because $IWC < 10^{-8}\,\text{kg}\,\text{m}^{-3}$, C_I may persist longer than C_0, C_1, or both.

5. Simulation Setup

This study investigates the impact of intersecting contrails on their lifetime. To establish a reference scenario (see Section 6.1), the lifetimes of two contrails, C_0 and C_1, are calculated independently, using the model described in Section 3. Subsequently, two

overlapping contrails are simulated according to the initial scenarios S_1 to S_3, and their life cycles with an influence on the lifetime are analyzed.

In each scenario, contrails behind two Airbus A320 aircraft are simulated. C_O is always simulated at $\lambda = -50^\circ$ and $\varphi = 150^\circ$ in H = 10,500 m altitude.

A realistically modeled weather pattern by the Global Forecast System (GFS) from 16 February 2016, 12 p.m. is applied. Figure 4 demonstrates the distribution of humidity in the area of investigation. Turbulence in this area (with an impact on the diffusivities D_v, D_h, and D_s) has been calculated assuming a lognormal distribution of turbulence in the lower troposphere and upper stratosphere and a linear correlation between a logarithmic diagnostic turbulence value [55], such as the vertical velocity w [Pa s^{-1}], provided by the GFS resulting in an eddy dissipation rate $\varepsilon = 6 \cdot 10^{-2}$ m^2 s^{-3}.

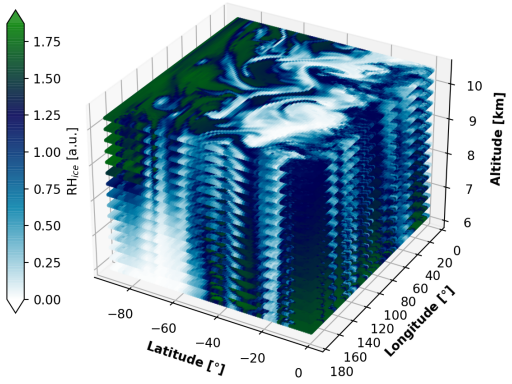

Figure 4. Relative humidity with respect to ice RH_{ice} modeled by the GFS for 16 February 2016, 12 p.m. Ice-supersaturated areas occur frequently in this region but are irregularly distributed in space. Below 8 km, there is a tendency to lower RH_{ice} values at the location of the contrail formation (at latitude −50 and longitude 150).

5.1. Initialization of Scenario S1

For a contrail embedded within another contrail with the same longitudinal alignment, two aircraft must fly sequentially along the same track and at the same altitude. To account for a realistic longitudinal separation [56], C_0 is generated 15 min before C_1 at the same altitude (H = 10,500 m) and with the same aircraft speed (220 m/s). Both contrails are formed at the study location (50° S, 150° E). Since the ice water content (IWC) is usually higher inside an existing contrail (here C_0) than in the surrounding atmosphere, the second contrail C_1 develops under favorable conditions, and its ice crystals grow rapidly.

5.2. Initialization of Scenario 2

Two overlapping contrails sharing the same longitudinal axes could be generated behind two aircraft flying along the same track, with a lateral separation, at the same altitude and with the same aircraft speed (220 m/s). C_0 is always formed at the study location 50° S, 150° E at H = 10,500 m. The model is run with different lateral separations between 2.5 NM and 130 NM. The minimum difference is in line with separation minima based on Air Traffic System (ATS) surveillance systems (using radar, Automatic Dependent Surveillance-Broadcast (ADS-B), or Multilateration (MLAT)) where the standard minimum separation prescribed by ICAO Doc 4444 of 5 NM may be reduced to 3 NM or 2.5 NM [57]. To ensure an overlap, contrail C_1 is generated at different time steps after C_0 has been formed. C_1 is always placed one horizontal standard deviation σ_h east of the centre C_0. Different levels of overlap are achieved by initiating C_1 with different longitudinal separations, as contrails initially diffuse very quickly in the lateral direction. The longitudinal

separation is varied between a few seconds and a little bit more than 100 min. Figure 5 gives an overview of the initial longitudinal and lateral separation values used in this study.

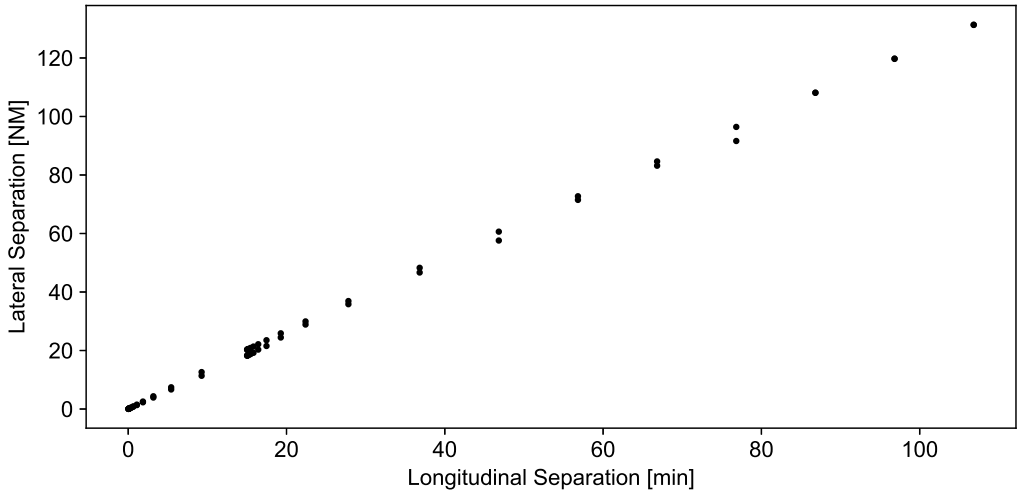

Figure 5. Set of simulations with varying initial longitudinal and lateral separations in scenario S2.

5.3. Initialization of Scenario 3

In the third scenario, the intersection angle α is varied: $\alpha \in [5°, 90°]$. The contrails C_0 and C_1 are formed at (H = 10,500 m) altitude with a speed of 220 m/s. C_0 is formed at the study location (50° S, 150° E), and C_1 is formed at 49.9868° S, 150.5253° E.

6. Results

6.1. S0: Contrail Microphysics and Lifetime Without Intersection

As a reference scenario *S*0, the lifetimes of two contrails C_0 and C_1 without intersection are modeled. To take into account the influence of the direction of flight (track), contrail C_1 is rotated by 45° in relation to C_0 (along the North–South axis)

Without intersection, C_0 and C_1 have similar lifetimes and live for t_{S0,C_0} = 653 min and t_{S0,C_1} = 638 min, corresponding to t_{S0,C_0} = 10.89 h and t_{S0,C_1} = 10.64 h, respectively. The differences in the lifetimes of the two contrails arise partly from the numerical and temporal resolution of the model and partly from slightly different atmospheric conditions resulting from the spatial rotation of C1 by 45°. Due to wind drift, both contrails are subject to lateral movement to the South–East (see Figure 6).

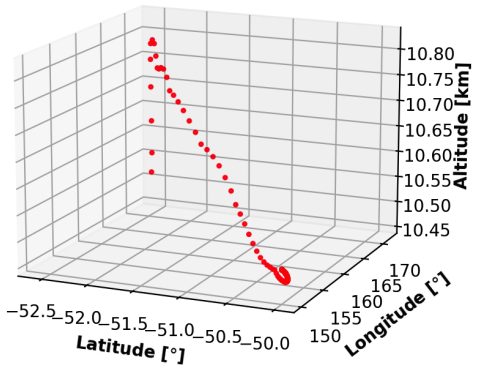

Figure 6. Contrail drift to the South–East during the contrails' lifetimes in scenario S0.

Both contrails die due to $rH_{ice} < 100\%$ (see Figure 7 top right). Without intersection, the mean ice particle radius r_p grows from 1 µm to 7.9 µm (Figure 7 top left). The initial sinking into less ice-saturated layers is due to a negative vertical wind and can be seen in

Figure 6. It causes a reduction in RH_{ice} and the associated IWC. Later, a vertical wind-induced upward movement and an increase in RH_{ice} and IWC can be seen before the ice crystals sink permanently from a radius of $r_p > 7.9$ µm and thus leave the ice-supersaturated layer (Figure 7 bottom left and Figure 6). Figure 7 clearly shows that the contrail cross-section CCS is independent of IWC, as the growth of the contrail depends solely on the turbulent diffusivities (see Equation (8)). Due to the absence of interaction between the two contrails in this reference scenario, the number of ice crystals remains constant.

The results also show that the microphysics and lifetime of the contrail are strongly dependent on external influences such as the degree of ice supersaturation, the vertical thickness of the ice-saturated layer, and the three-dimensional wind, and therefore cannot be standardized. The results of the reference scenario now allow a comparison of the microphysics and lifetimes of the contrails when they interact with each other by superposition under identical atmospheric conditions.

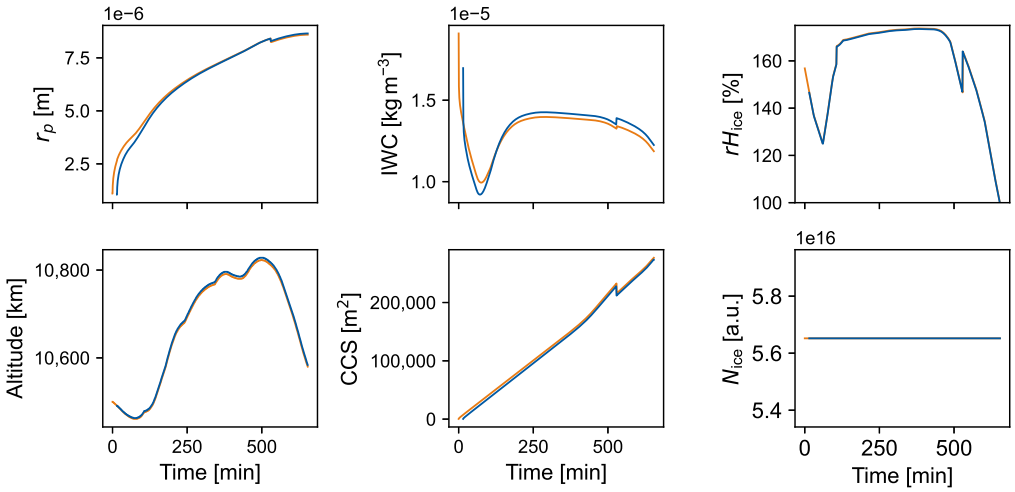

Figure 7. Contrail microphysics in the reference scenario S0 without intersection. C_0 (orange) is formed 15 min before C_1 (blue) at the same position but laterally rotated by 45°.

6.2. S1: Microphysics and Lifetime of an Embedded Contrail System

If one contrail is embedded in another contrail, as described in S1 in Figure 2, the amount of IWC added to the inner contrail C_1 during growth is limited because the intersection part only receives a proportionate amount of ice water and ice particles from the contrail C_0 according to the overlapping volumes. However, as the volumes increase at the same time, IWC in the intersection part generally decreases, while the number of particles increases slightly. For this reason, the intersection part is likely to die very soon due to $IWC < 10^{-8}$ kg m^{-3}. However, it is not only the added humidity that is decisive for the lifetime. If the contrails grow slowly (e.g., due to less turbulence in the atmosphere), the ice water content decreases less quickly. A long lifetime is expected if the (compact) contrails are kept in the ice-saturated layer by updrafts. The intersection part can then outlive the original contrails.

In Scenario 1, the deficit of IWC is maximized for C_1. For this reason, the lifetime of C_1 is very short ($t_{S1,C_0} = 105$ min $= 1.76$ h) compared to C_0 $t_{S1,C_1} = 650$ min$= 10.84$ h.

The particles in the intersection part only reach a radius of $r_p = 1$ µm (see Figure 8) because IWC rapidly decreases and converges towards the lower limit to be considered optically effective, whereas the number of ice particles N_{ice} increases at the cost of C_0. Note the difference in altitude, caused by the difference in mean ice particle radius r_p (Figure 8, bottom, left). The difference in the altitude of roughly 100 m and the lack of humidity for the inner contrail C_1 causes different causes of sublimation for both contrails. While C_I dies

of $IWC < 10^{-8}$ kg m^{-3} (see Figure 8, top, middle), C_0 leaves the ice-supersaturated layer after a long lifetime.

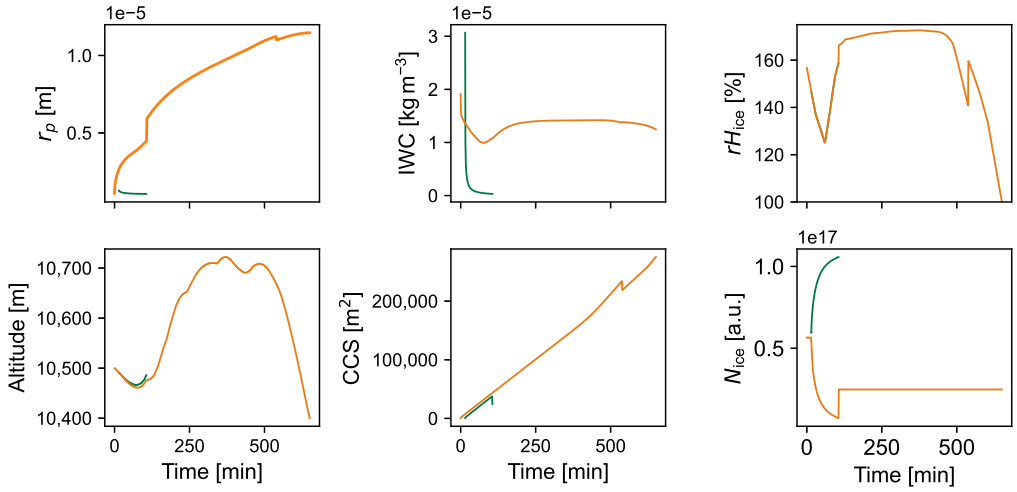

Figure 8. Microphysics of two embedded, parallel contrails: $C_1 = C_I$ (green) forms within C_0 (orange), as described in scenario S1.

6.3. Microphysics and Lifetimes of Two Parallel Overlapping Contrails

If two parallel contrails intersect in such a way that both still have an outside (S2), the contrails are supplied with ice-saturated humidity via the outer surfaces, IWC can increase, the ice crystals can grow, and both contrails can live for a long time. It follows from this that parallel overlapping does not reduce the contrail lifetime. The intersection part, on the other hand, is expected to sublime quickly. This phenomenon can be seen in Figure 9, where the longest contrail lifetime of $t_{S2,C_0} = 11.55$ h = 41,472 s.

Due to an early intersection, the intersecting volume increases rapidly (see bottom center in Figure 9), resulting in a large number of particles in the overlapping region (bottom right in Figure 9). Because no external moisture is supplied to the intersection part, IWC_{CI} decreases rapidly (see top center of Figure 9). Over its relatively long lifetime of $t_{S2,C_I} = 6.69$ h, the overlapping region inhibits the growth of ice crystals in the two outer contrails (see top left of Figure 9). As a result, the crystals remain within the ice-supersaturated layer for an extended period before eventually descending under their own weight.

In the case of a parallel intersection, the ratio between the overlapping area to the area of each ellipse remains constant due to the symmetric growth of the elliptical cross-sections. This causes the ice particles to grow in a similar way, resulting in nearly the same geometric altitude. The cross-sections of C_0 and C_1 also grow similarly. As expected, the intersection part dies due to $IWC < 10^{-8}$ kg m^{-3}, while C_0 and C_1 again dissipate due to $rH_{ice} < 100\%$.

Slower ice crystal growth and smaller crystal sizes lead to longer contrail lifetimes, as the crystals remain within the ice-supersaturated layer for a longer period due to the updraft and settle more slowly [40,49]. In the case of overlapping contrails, the lifetime of C_0 can therefore be expected to depend on the intersection volume, as this volume determines how many ice crystals are shared between the two contrails and are thus no longer available to each individual plume.

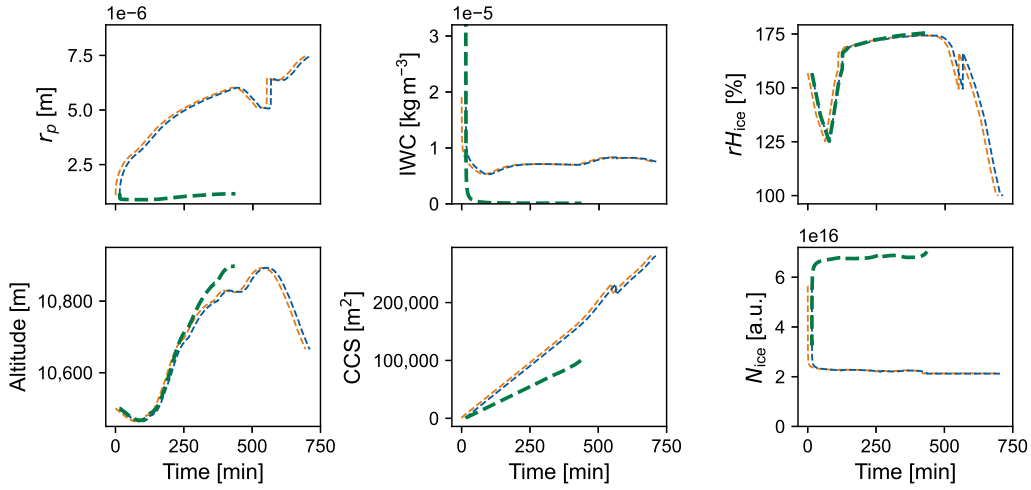

Figure 9. Microphysics of two long-living parallel contrails (C_0 (orange), C_1 (blue) and C_I (green)) intersecting at the very beginning.

At the same time, a large overlap reduces the exposed outer surface area through which the contrails can take up ice-supersaturated air, which further slows crystal growth (compare the particle radii in Figures 8 and 9). Consequently, ice crystal growth appears to depend not only on the volume ratio between C_0 or C_1 and C_I but also on the available outer surface area able to absorb supersaturated air. However, the complexity of the problem, compounded by four-dimensional and only partially predictable atmospheric boundary conditions, limits the identification of clear lifetime indicators in the simulations.

Figure 10 shows that the maximum distance between the contrails exhibits an influence on their lifetime when compared with the horizontal standard deviation of C_0. Smaller maximum distances correspond to longer lifetimes. This means that a parallel overlap increases the contrail lifetime. This relationship is considerably clearer than the effect of overlapping volume (absolute or relative) or overlapping area on contrail lifetime.

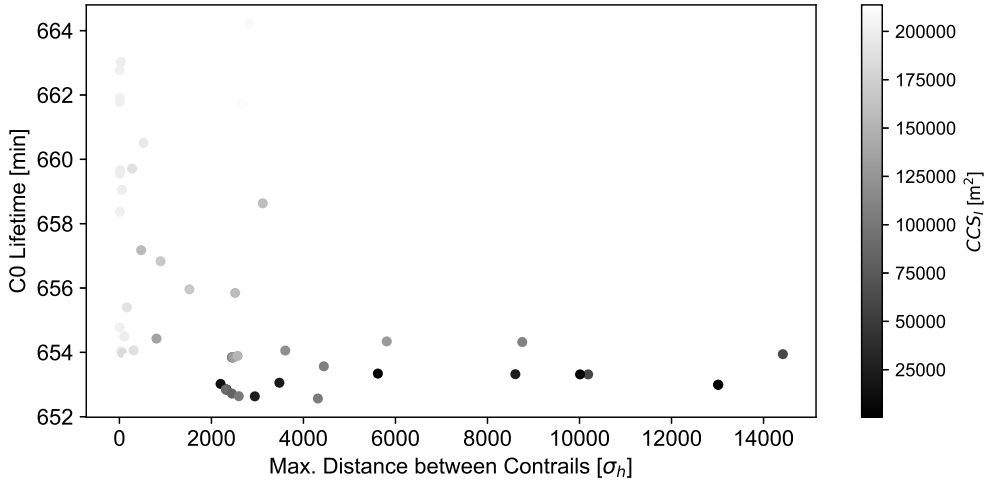

Figure 10. Decreasing lifetime with increasing maximum distance between two intersecting contrails. Note that the shortest lifetime $t_{S2,C0} = 10.89$ h (=653 min) corresponds to non-overlapping contrails.

There is a further correlation between the time that C_1 is generated after C_0 and the lifetime. Here, the later that C_1 is generated, the shorter the lifetime of C_1 and C_0, because the slower C_0 grows, the smaller the overlap volume and the fewer the number of ice crystals transferred from C_1 to C_I.

In addition, the timing of the maximum intersection between the two contrails has a direct impact on the lifetime of C_0 (Figure 11). If the intersection occurs at a later stage of contrail evolution, the resulting intersection area remains small due to the limited spatial overlap. Consequently, the transfer of ice crystals is reduced, leading to a shorter lifetime of C_0. In contrast, earlier intersections are associated with larger overlap volumes and therefore tend to promote longer-lived contrails.

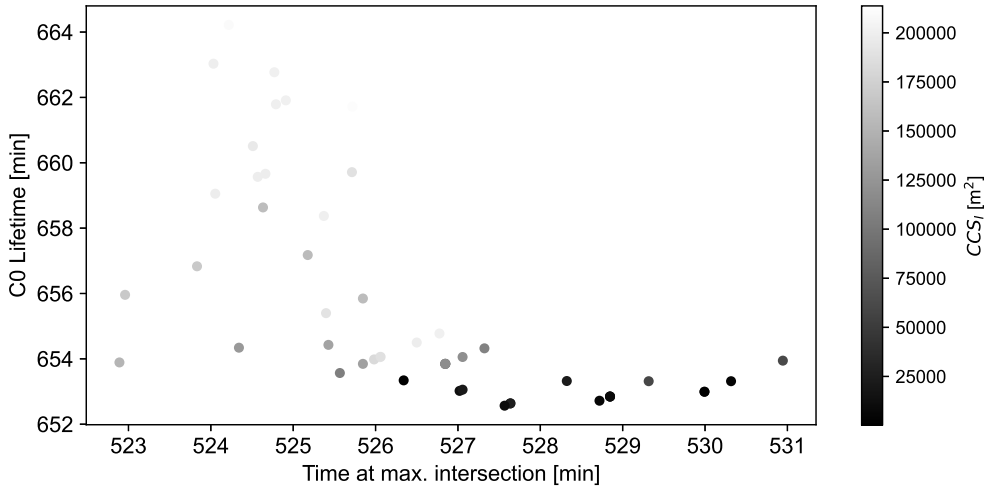

Figure 11. Impact of the time at maximum intersection on the lifetime of C_0. Late intersections result in small intersection areas and shorter lifetimes.

6.4. Microphysics and Lifetime of Two Arbitrary Overlapping Contrails

If two contrails intersect at an angle $\alpha > 0°$, the lifetime is surprisingly only weakly dependent on the angle α. As shown in Figures 12 and 13, the lifetime of the original contrails with $\alpha = 45°$ and $\alpha = 90°$ is almost identical with $t_{S3,C_0} = 40{,}438$ s and $t_{S3,C_1} = 39{,}538$ s, corresponding to $t_{S3,C_0} = 11.23$ h and $t_{S3,C_1} = 10.98$ h.

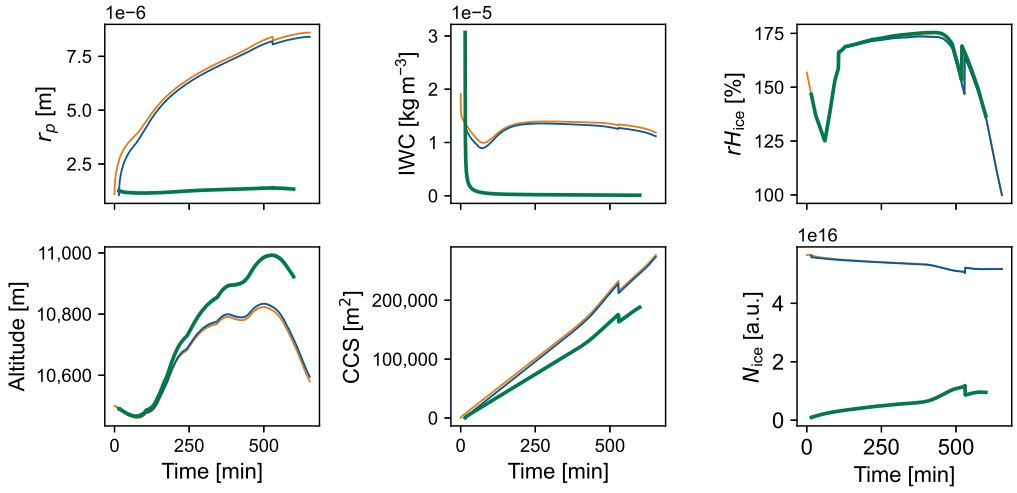

Figure 12. Contrail microphysics in scenario S3. Contrail C_1 (blue) intersects C_0 (orange) with an angle of $\alpha = 45°$. C_I is shown as a green line.

Even the interception part C_I lives for almost the same amount of time: $t_{S3,C_I} = 28{,}776$ s ($t_{S3,C_I} = 7.99$ h). However, the impact of the intersection angle α becomes clear in the C_I cross-section and the number of particles $N_{ice}(C_I)$ (Figures 12 and 13, bottom). At $\alpha = 90°$, the cross-section grows more slowly and C_I dies with a cross-section of

$CCS_{\alpha=90} = 101{,}079\ \mathrm{m}^2$ compared to $CCS_{\alpha=45} = 174{,}076\ \mathrm{m}^2$. The number of particles in C_I increases more slowly at $\alpha = 90°$ and only reaches $N_{\mathrm{ice}} = 4.27 \times 10^{15}$ at the end of the lifetime compared to $N_{\mathrm{ice}} = 8.63 \times 10^{15}$ at $\alpha = 45°$. The impact of α on the intersection cross-section can also be seen in Figure 3.

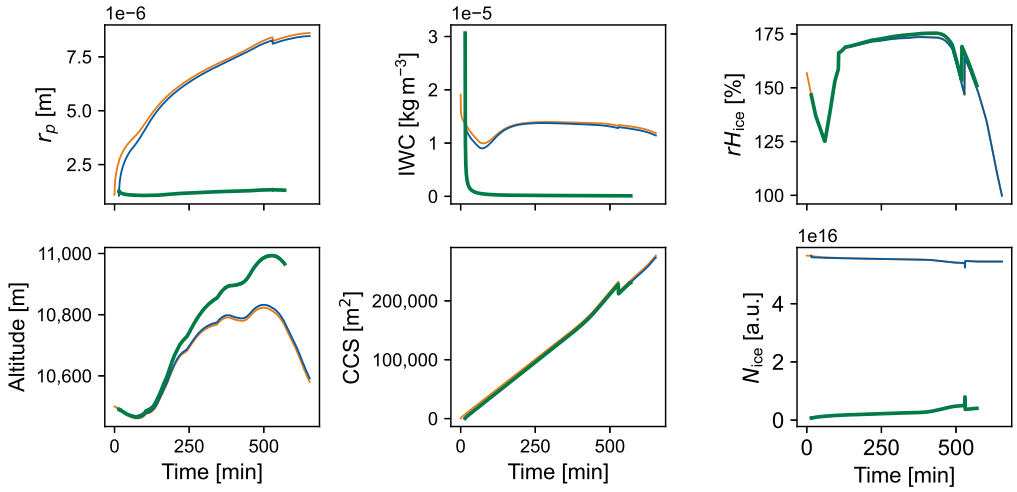

Figure 13. Contrail microphysics in scenario S3. Contrail C_1 (blue) intersects C_0 (orange) with an angle of $\alpha = 90°$. The green line represents C_I.

The impact of α on the contrail microphysics is limited because the intersection volume is reduced to a single contrail section and therefore small, compared to the entire contrail. Regardless of α, C_I again dies due to $IWC < 10^{-8}\ \mathrm{kg\,m^{-3}}$, whereas C_0 and C_1 die due to ice under-saturation ($rH_{\mathrm{ice}} < 100\%$). Table 1 represents a few example lifetimes of C_1 for different intersection angles.

Table 1. Influence of the intersection angle α of two intersecting contrails (as described in S3) on the lifetime of the overlapping part C_I. While the lifetime of the overlap region depends on the intersection angle, the lifetimes of the individual contrails are largely independent of this angle ($t_{C_1} = 38{,}267\ \mathrm{s} \approx 10.63\ \mathrm{h}$ and $t_{C_0} = 39{,}167\ \mathrm{s} \approx 10.88\ \mathrm{h}$).

Angle α	t_{C_I} [hh:mm]
10°	10:08
20°	10:03
30°	09:56
40°	09:52
50°	09:47
60°	09:43
70°	09:39
80°	09:26
90°	09:17

The impact of the intersection angle α on the contrail lifetime is surprisingly low. However, caused by different cross-sections of C_I and numbers of ice particles in C_I, the impact of α on the optical properties remains exciting.

7. Summary and Conclusions

The objective of this investigation is to assess how intersecting contrails influence each other's lifetimes. As a reference case, the independent lifetimes of two non-intersecting contrails, denoted as C_0 and C_1, are first determined. Subsequently, the lifetimes of these

two contrails are analyzed for a range of intersection angles and intersection positions under otherwise identical atmospheric conditions. In scenarios S1 and S3, C_0 is always initiated 15 min earlier than C_1 at the same flight altitude.

Overall, the results show that contrail lifetimes tend to be shortened once contrails intersect, because the amount of ambient humidity available to each individual contrail during its lifetime is reduced. The closer the contrails are to each other, that is, the larger the intersection volume, the stronger this effect becomes. In all investigated scenarios, the intersection part C_I dissipates first due to a local lack of ice water content.

Among the investigated cases, scenario 2, in which two contrails overlap in parallel, proved to be the most interesting. In this configuration, the contrail lifetime was extended compared to other intersection scenarios, while the overlapping part reached the largest volumes and exerted the strongest influence on the overall contrail evolution. A particularly notable result is that, in scenario 2, the second-generated contrail C_1 dissipates at the same time as the older contrail C_0. This indicates that contrail lifetime depends more strongly on the prevailing atmospheric conditions than on the specific intersection geometry itself.

Although the direct impact of the intersection on contrail lifetime is relatively small for the case of only two overlapping contrails, this finding is highly relevant for real atmospheric conditions. In reality, tens of contrails often overlap simultaneously within highly trafficked airspaces. Such multiple overlapping interactions are expected to amplify the effects observed here and may lead to a considerably stronger influence on contrail lifetime and climate impact.

In this study, the model is applied to a single global weather data set. From this, it follows that the atmospheric state variables remain constant over time. This unrealistic assumption has an impact on the contrails' lifetimes. First, in the respective atmospheric layer, ice supersaturation is assumed over an unrealistic long period. In this context, the contrails cannot die because the ice-supersaturated layer dissolves or moves away from the contrail. Furthermore, a constant atmospheric turbulence of $\varepsilon = 6 \cdot 10^{-2}\ \mathrm{m^2\,s^{-3}}$ is assumed over the entire period, which creates ideal conditions for long-lasting contrails, regardless of the thermal effects caused by the time of day. Due to these circumstances, a comparison of the lifetimes of different contrails (by minimizing external effects) can be ensured, but very long lifetimes will be obtained.

In extended studies, time-varying weather scenarios will be considered and discrete weather data over time will be interpolated. Here, good experience with the Kriging approach had been made for this purpose [58].

In the case of a weakly ice-supersaturated atmosphere, the heat emitted by a crossing aircraft can locally sublimate the older contrail. The heat $Q = 43\ \mathrm{MJ\,kg^{-1}}$

$$Q = c_p\, m\, \Delta T \tag{41}$$

emitted by the engine per kilogram of fuel burned contributes to a temperature increase ΔT [K], which in turn both reduces the ice supersaturation and influences the difference to the critical temperature in the Schmidt–Appleman criterion. In Equation (41), c_p denotes the specific heat capacity of ice-supersaturated air ($c_p(T = 220\ \mathrm{K}) = 1710\ \mathrm{J\,(K\,kg)^{-1}}$ [59]) and m describes the mass of air, emitted per second by all aircraft engines ($m \approx 100\ \mathrm{kg\,s^{-1}}$ for an CFM56 engine of an A320 in cruise [60]). This effect has not been investigated so far, as the study has been limited to highly ice-supersaturated areas. In future work, critical ambient temperatures and humidity values that lead to the sublimation of older contrails by younger ones are to be identified.

This study will be continued by means of optical investigations. The impact of intersected contrails on their optical properties will be analyzed by extending the opti-

cal single-contrail model https://github.com/jro-github/rf-contrails [61] (accessed on 1 September 2025) to "clustered" contrails.

Author Contributions: Conceptualization, J.R.; methodology, J.R. and M.L.; software, J.R. and M.L.; validation, J.R. and M.L.; formal analysis, J.R.; investigation, J.R.; resources, J.R.; data curation, J.R.; writing—original draft preparation, J.R. and M.L.; writing—review and editing, J.R.; visualization, J.R.; supervision, J.R.; project administration, J.R.; funding acquisition, J.R. All authors have read and agreed to the published version of the manuscript.

Funding: This research did not receive any external funding. Both authors conducted this study in addition to their regular, funded work. The major part of the work was completed while both authors were affiliated with the Technical University of Dresden.

Data Availability Statement: The original contributions presented in the study are included in the article, further inquiries can be directed to the corresponding author. The source code and an example data set is openly available https://github.com/jro-github/intersected_contrails/tree/main (accessed on 1 November 2025), licensed under Apache-2.0.

Acknowledgments: We sincerely thank the three reviewers for their extremely helpful and constructive feedback, as well as for their valuable suggestions for improvement and correction. This research is part of the project ICATO (Individual Condensation Trails in Aircraft Trajectory Optimization) founded by Judith Rosenow.

Conflicts of Interest: The authors declare no conflicts of interest.

References

1. Lee, D.S.; Pitari, G.; Grewe, V.; Gierens, K.; Penner, J.E.; Petzold, A.; Prather, M.J.; Schumann, U.; Bais, A.; Berntsen, T.; et al. Transport impacts on atmosphere and climate: Aviation. *Atmos. Environ.* **2010**, *44*, 4678–4734. [CrossRef] [PubMed]
2. Lee, D.; Fahey, D.; Skowron, A.; Allen, M.; Burkhardt, U.; Chen, Q.; Doherty, S.; Freeman, S.; Forster, P.; Fuglestvedt, J.; et al. The contribution of global aviation to anthropogenic climate forcing for 2000 to 2018. *Atmos. Environ.* **2021**, *244*, 117834. [CrossRef]
3. Brewer, A.W. Condensation trails. *Weather* **1946**, *1*, 34–40. [CrossRef]
4. Burkhardt, U.; Kärcher, B.; Schumann, U. Global Modeling of the Contrail and Contrail Cirrus Climate Impact. *Am. Meteorol. Soc.* **2010**, *91*, 479–484. [CrossRef]
5. Sarna, A.; Meijer, V.; Chevallier, R.; Duncan, A.; McConnaughay, K.; Geraedts, S.; McCloskey, K. Benchmarking and improving algorithms for attributing satellite-observed contrails to flights. *Atmos. Meas. Tech.* **2025**, *18*, 3495–3532. [CrossRef]
6. Jafarimoghaddam, A.; Soler, M. A Multi-Physics Eulerian Framework for Long-Term Contrail Evolution. *arXiv* **2025**, arXiv:2509.00965.
7. Rosenow, J.; Hospodka, J.; Lán, S.; Fricke, H. Validation of a Contrail Life-Cycle Model in Central Europe. *Sustainability* **2023**, *15*, 8669. [CrossRef]
8. Vázquez-Navarro, M.; Mannstein, H.; Mayer, B. An automatic contrail tracking algorithm. *Atmos. Meas. Tech.* **2010**, *3*, 1089–1101. [CrossRef]
9. Mannstein, H.; Vázquez-Navarro, M.; Graf, K.; Duda, D.; Schumann, U. Contrail Detection in Satellite Images. In *Atmospheric Physics: Background-Methods-Trends*; Springer: Berlin, Germany, 2012; pp. 433–447. [CrossRef]
10. Zhang, G.; Zhang, J.; Shang, J. Contrail Recognition with Convolutional Neural Network and Contrail Parameterizations Evaluation. *Sola* **2018**, *14*, 132–137. [CrossRef]
11. Duda, D.P.; Bedka, S.T.; Minnis, P.; Spangenberg, D.; Khlopenkov, K.; Chee, T.; Smith, W.L., Jr. Northern Hemisphere contrail properties derived from Terra and Aqua MODIS data for 2006 and 2012. *Atmos. Chem. Phys.* **2019**, *19*, 5313–5330. [CrossRef]
12. McCloskey, K.; Geraedts, S.; Van Arsdale, C.; Brand, E. A human-labeled Landsat-8 contrails dataset. In *Proceedings of the ICML 2021 Workshop on Tackling Climate Change with Machine Learning*; ACM, Inc.: New York, NY, USA, 2021.
13. Teoh, R.; Engberg, Z.; Schumann, U.; Voigt, C.; Shapiro, M.; Rohs, S.; Stettler, M.E.J. Global aviation contrail climate effects from 2019 to 2021. *Atmos. Chem. Phys.* **2024**, *24*, 6071–6093. [CrossRef]
14. Jarry, G.; Very, P.; Heffar, A. Deep Semantic Contrails Segmentation of GOES-16 Satellite Images: A Hyperparameter Exploration. In Proceedings of the SESAR Innovation Days (SID 2024), Rome, Italy, 12–15 November 2024.
15. Wang, Z.; Bugliaro, L.; Jurkat-Witschas, T.; Heller, R.; Burkhardt, U.; Ziereis, H.; Dekoutsidis, G.; Wirth, M.; Groß, S.; Kirschler, S.; et al. Observations of microphysical properties and radiative effects of contrail cirrus and natural cirrus over the North Atlantic. *Atmos. Chem. Phys. Discuss.* **2022**, *2022*, 1–36. [CrossRef]

16. Geraedts, S.; Brand, E.; Dean, T.R.; Eastham, S.; Elkin, C.; Engberg, Z.; Hager, U.; Langmore, I.; McCloskey, K.; Yue-Hei Ng, J.; et al. A scalable system to measure contrail formation on a per-flight basis. *Environ. Res. Commun.* **2024**, *6*, 015008. [CrossRef]
17. Wang, Z. Combining UPerNet and ConvNeXt for Contrails Identification to reduce Global Warming. *arXiv* **2023**, arXiv:2310.04808.
18. Schumann, U. A contrail cirrus prediction tool. In Proceedings of the International Conference on Transport, Atmosphere and Climate, DLR/EUR, Aachen, Germany; Maastricht, The Netherlands, 22–25 June 2009.
19. Schumann, U.; Heymsfield, A. On the lifecycle of individual contrails and contrail cirrus. *AMS Meteorol. Monogr.* **2017**, *58*, 3.1–3.24. [CrossRef]
20. Cantin, S.; Chouak, M.; Morency, F.; Garnier, F. Eulerian–Lagrangian CFD-microphysics modeling of a near-field contrail from a realistic turbofan. *Int. J. Engine Res.* **2022**, *23*, 661–677. [CrossRef]
21. Pauen, J.; Unterstrasser, S.; Stephan, A. Towards refined contrail simulations of formation flight scenarios. In Proceedings of the 34th ICAS Congress 2024, Florence, Italy, 9–13 September 2024.
22. Ramsay, J.; Tristanto, I.; Shahpar, S.; John, A. Assessing the Environmental Impact of Aircraft/Engine Integration with Respect to Contrails. *J. Eng. Gas Turbines Power* **2024**, *146*, 111026. [CrossRef]
23. Jones, H.M.; Haywood, J.; Marenco, F.; O'Sullivan, D.; Meyer, J.; Thorpe, R.; Gallagher, M.W.; Krämer, M.; Bower, K.N.; Rädel, G.; et al. A methodology for in-situ and remote sensing of microphysical and radiative properties of contrails as they evolve into cirrus. *Atmos. Chem. Phys.* **2012**, *12*, 8157–8175. [CrossRef]
24. Spinhirne, J.; Hart, W.; Duda, D. Evolution of the morphology and microphysics of contrail cirrus from airborne remote sensing. *Geophys. Res. Lett.* **1998**, *25*, 1153–1156. [CrossRef]
25. Rap, A.; Forster, P.M.; Haywood, J.M.; Jones, A.; Boucher, O. Estimating the climate impact of linear contrails using the UK Met Office climate model. *Geophys. Res. Lett.* **2010**, *37*, L20703. [CrossRef]
26. Vogel, F.; Lacher, L.; Nadolny, J.; Saathoff, H.; Leisner, T.; Möhler, O. Development and validation of a new cloud simulation experiment for lab-based aerosol–cloud studies. *Rev. Sci. Instrum.* **2022**, *93*, 095106. [CrossRef] [PubMed]
27. Kärcher, B. Formation and radiative forcing of contrail cirrus. *Nat. Commun.* **2018**, *9*, 1824. [CrossRef]
28. Teoh, R.; Schumann, U.; Stettler, M.E.J. Beyond Contrail Avoidance: Efficacy of Flight Altitude Changes to Minimise Contrail Climate Forcing. *Aerospace* **2020**, *7*, 121. [CrossRef]
29. Spichtinger, P.; Gierens, K.M.; Read, W. The global distribution of ice-supersaturated regions as seen by the Microwave Limb Sounder. *Q. J. R. Meteorol. Soc.* **2003**, *129*, 3391–3410. [CrossRef]
30. Kärcher, B.; Corcos, M. On the Lifetimes of Persistent Contrails and Contrail Cirrus. *J. Geophys. Res. Atmos.* **2025**, *130*, e2025JD044488. [CrossRef]
31. Kaufmann, S.; Dischl, R.; Voigt, C. Regional and seasonal impact of hydrogen propulsion systems on potential contrail cirrus cover. *Atmos. Environ. X* **2024**, *24*, 100298. [CrossRef]
32. Narciso, M.; Melo de Sousa, J. Influence of Sustainable Aviation Fuels on the Formation of Contrails and Their Properties. *Energies* **2021**, *14*, 5557. [CrossRef]
33. Tasca, A.L.; Cipolla, V.; Abu Salem, K.; Puccini, M. Innovative Box-Wing Aircraft: Emissions and Climate Change. *Sustainability* **2021**, *13*, 3282. [CrossRef]
34. Yin, F.; Volker, G.; Gierens, K. Impact of Hybrid-Electric Aircraft on Contrail Coverage. *Aerospace* **2020**, *7*, 147. [CrossRef]
35. Baneshi, F.; Cerezo-Magaña, M.; Soler, M. Integrating Non-CO_2 climate impact considerations in air traffic management: Opportunities and challenges. *Transp. Policy* **2024**, *155*, 274–286. [CrossRef]
36. Rosenow, J.H.; Fricke, H. Validation of a Contrail Life Cycle model in Central Europe. *Aerospace* 2026, *submitted*.
37. Schumann, U.; Konopka, P.; Baumann, R.; Busen, R.; Gerz, T.; Schlager, D.; Schulte, P.; Volkert, H. Estimate of diffusion parameters of aircraft exhaust plumes near the tropopause from nitric oxide and turbulence measurements. *J. Geophys. Res.* **1995**, *100*, 14147–14162. [CrossRef]
38. Paugam, R.; Paoli, R.; Cariolle, D. Influence of vortex dynamics and atmospheric turbulence on the early evolution of a contrail. *Atmos. Chem. Phys.* **2010**, *10*, 3933–3952. [CrossRef]
39. Holzäpfel, F. Probabilistic Two-Phase Wake Vortex Decay and Transport Model. *J. Aircr.* **2003**, *40*, 323. [CrossRef]
40. Rosenow, J. Optical Properties of Condenstation Trails. Ph.D. Thesis, Technische Universität Dresden, Dresden, Germany, 2016.
41. Merziger, G.; Mühlbach, G.; Wille, D.; Wirth, T. *Formeln + Hilfen zur Höheren Mathematik*; Binomi Verlag Hannover: Springe, Germany, 2001.
42. Sonntag, D. Advancements in Field Hygrometry, Review Article. *Meteorol. Z.* **1994**, *3*, 51–66. [CrossRef]
43. Myhre, G.; Shindell, D.; Bréon, F.M.; Collins, W.; Fuglestvedt, J.; Huang, J.; Koch, D.; Lamarque, J.F.; Lee, D.; Mendoza, B.; et al. Anthropogenic and Natural Radiative Forcing. In *Climate Change 2013: The Physical Science Basis. Contribution of Working Group I to the Fifth Assessment Report of the Intergovernmental Panel on Climate Change*; Cambridge University Press: Cambridge, MA, USA, 2013.
44. Kraus, H. *Die Atmosphäre der Erde*; Springer: Berlin/Heidelberg, Germany, 2001.

45. Sussmann, R.; Gierens, K.M. Lidar and numerical studies on the different evolution of vortex pair and secondary wake in young contrails. *J. Geophys. Res.* **1999**, *104*, 2131–2142. [CrossRef]
46. Connolly, P.J.; Emersic, C.; Field, P.R. A laboratory investigation into the aggregation efficiency of small ice crystals. *Atmos. Chem. Phys.* **2011**, *12*, 2055–2076. [CrossRef]
47. Stokes, G.G. On the effect of internal friction of fluids on the motion of pendulums. *Trans. Camb. Philos. Soc.* **1851**, *9*, 1–86.
48. Roedel, W. *Physik Unserer Umwelt, die Atmosphäre*; Springer: Berlin/Heidelberg, Germany, 2000.
49. Rosenow, J.; Köhler, S.; Geyer, T. Impact of Alternative Propulsion on Contrail Formation and Lifetime. *Aerospace* **2025**.
50. Robusto, C.C. The cosine-haversine formula. *Am. Math. Mon.* **1957**, *64*, 38–40. [CrossRef]
51. Schumann, U.; Graf, K.; Mannstein, H.; Mayer, B. *Atmospheric Physics*; Springer: Berlin/Heidelberg, Germany, 2012.
52. Moffatt, H.K. Statistical Fluid Mechanics: The Mechanics of Turbulence, volume 1. By A. S. MONIN and A. M. YAGLOM. M. I. T. Press, 1971. 769 pp. £10.50. *J. Fluid Mech.* **1973**, *60*, 410–416. [CrossRef]
53. Schröder, F.; Kärcher, B.; Duroure, C.; Ström, J.; Petzold, A.; Gayet, J.F.; Strauss, B.; Wendling, P.; Borrmann, S. On the Transition of Contrails into Cirrus Clouds. *J. Atmos. Sci.* **2000**, *57*, 464–480. [CrossRef]
54. Atlas, D.; Wang, Z.; Duda, D. Contrails to Cirrus—Morphology, Microphysics, and Radiative Properties. *J. Appl. Meteorol. Climatol.* **2006**, *45*, 5–19. [CrossRef]
55. Sharman, R.D.; Pearson, J.M. Prediction of Energy Dissipation Rates for Aviation Turbulence. Part I: Forecasting Nonconvective Turbulence. *J. Appl. Meteorol. Climatol.* **2017**, *56*, 317–337. [CrossRef]
56. International Civil Aviation Organization. *Doc 9426 Air Traffic Service Planning Manual*; Annex 11 to the Convention on International Civil Aviation; International Civil Aviation Organization: Montreal, QC, Canada, 1984.
57. International Civil Aviation Organization. *Doc. 4444 PANS-ATM*; Procedures of Air Navigation Services, Air Traffic Management. International Civil Aviation Organization: Montreal, QC, Canada, 2016.
58. Chen, G.; Fricke, H.; Okhrin, O.; Rosenow, J. Importance of Weather Conditions in a Flight Corridor. *Stats* **2022**, *5*, 312–338. [CrossRef]
59. Marquet, P. On the computation of moist-air specific thermal enthalpy: Moist-air Specific Thermal Enthalpy. *Q. J. R. Meteorol. Soc.* **2015**, *141*, 67–84. [CrossRef]
60. Rosenow, J.; Chen, G.; Fricke, H.; Wang, Y. Factors Impacting Chinese and European Vertical Fight Efficiency. *Aerospace* **2022**, *9*, 76. [CrossRef]
61. Rosenow, J.; Fricke, H. When do contrails cool the atmosphere? In Proceedings of the SESAR Innovation Days (SID 2022), Budapest, Hungary, 5–8 December 2022.